International Journal for Housing Science and Its Applications
Publish August 10, 2025. Volume 46, Issue 4 Pages 726-735

https://doi.org/10.70517/ijhsa46466

Changes in anatomical structure of reed root system under different water level conditions analyzed based on image processing algorithm

Mingyu Zhang[1] and Zhenwen Xu[1,*]
[1] College of Geographical Sciences, Changchun Normal University, Changchun, Jilin, 130032, China
Corresponding authors: (e-mail: xzw997799@163.com).

Abstract Accurate observation of the anatomical structure of the root system of aquatic plants is of great significance in understanding their adaptive mechanisms. In this paper, an image processing algorithm based on improved Retinex theory is proposed to address the problem of poor image quality and blurred details of underwater reed root system. The method combines the light-directed variable attention module (LDAT), the spatial-frequency domain feature fusion module (SDFF), and the medium transport module (MTM), and realizes the effective enhancement of the underwater image by introducing a perturbation term to simulate the underwater imaging environment and using saturation to distinguish between the artificial illumination and the natural light source. The experimental results show that compared with the traditional dark channel a priori algorithm and MSR algorithm, the algorithm in this paper improves the information entropy significantly, in which the information entropy of image 3 is improved from 6.762 to 7.827, and the standard deviation is increased from 18.978 to 58.973, and the average running time is only 6.696 s, which is significantly better than that of the dark channel a priori algorithm, which is 71.49 s. The anatomical structure of the root system is analyzed for the reeds under the different water depth conditions. By analyzing the anatomical structure of the root system under different water depth conditions, it was found that the proportion of root cortex aerated tissues was significantly positively correlated with the water depth, and the proportion of aerated tissues was significantly larger under deep flooding than non-flooding conditions. The conclusion shows that the algorithm can effectively improve the quality of underwater images and provide technical support for the accurate analysis of plant root structure.

Index Terms Image processing algorithm, Retinex theory, underwater image enhancement, reed root system, anatomical structure, information entropy

I. Introduction

Wetlands are known as the "kidneys of nature" because of their great ecological value, environmental and productive functions. However, the current rapid development of modern civilization has brought about serious destructive impacts on this precious natural resource. For example, urbanization, agriculture, industry and other factors such as the reduction of marsh area or the decline of vegetation cover brought about by agricultural land reclamation have weakened the self-healing ability of wetlands or even completely lost this potential, which has led to a series of discussions on how to ensure that they can continue to play the important functions they should be [1]-[3].

Wetland plants are plants adapted to grow in wet environments, and they are often characterized by adaptations to moisture infiltration and muddy soils, of which reed is one [4]. It constitutes a key element of the wetland ecosystem with other plants, and their combination with the topography forms a variety of spatial hierarchies, providing various types of ecological environments for wetland organisms to live in and search for food in order to satisfy the survival needs of all kinds of living organisms, which builds up a diversified and complex wetland ecosystem [5], [6]. Reed has a high biomass and availability, can be used as an important raw material such as paper, but also building materials, pharmaceutical raw materials and many other uses, has a wide range of application value, but also has a purification of the environment, such as nitrogen, phosphorus and other nutrients, as well as cadmium and other heavy metals have a strong adsorption and removal capacity [7]-[9]. By virtue of its excellent resistance, wide living space adaptability and rapid growth characteristics and strong reproduction strength, reed has become a key plant species for ecological environment restoration, and plays a key role in the protection of wetland biodiversity, and maintains the normal functioning and stability of wetland ecosystems [10]-[12].

The study of plant anatomical structure helps to understand the absorption, conduction, storage and support functions of plant organs, the growth and development process of plants, as well as the changes in different environmental conditions, which can reveal the mechanism of plant adaptation to various growth environments and provide a theoretical basis for plant genetic improvement and planting pattern selection [13]-[15]. In recent years, the hydrological pattern of wetlands has changed due to climate change [16]. Therefore, the adaptation of wetland ecosystems can be reflected by analyzing the changes in the root structure of reed.

In this study, a processing algorithm framework for underwater reed root images is constructed based on the improved Retinex theory. Through the introduction of light-guided variable attention module to enhance the perception of dark light areas, the design of air-frequency domain feature fusion module to improve the recovery ability of underwater image distortion, and the combination of media transmission module to optimize the image enhancement effect. On this basis, we systematically analyze the changing law of the anatomical structure of reed root system under different water level conditions, and explore its physiological adaptation mechanism, so as to provide scientific basis for the protection and management of wetland ecosystem.

II. Retinex-based image processing algorithm for underwater reed root system

II. A. Underwater graphics processing techniques

In haze-free natural images, there are always pixels with at least one color channel close to zero, and the a priori theory of dark channels for atmospheric denoising algorithms is investigated.

$$I(x) = J(x)t(x) + A\left(1 - t(x)\right) \tag{1}$$

In this case, $I(x)$ denotes the atmospheric image affected by haze, $J(x)$ denotes the atmospheric image without haze interference, $t(x)$ denotes the transmittance, i.e., the rate at which light reaches the camera without being scattered or absorbed, and A denotes the global atmospheric light. Further studies have shown that this phenomenon also applies to underwater images. The difference, however, is that water and suspended particles in the water absorb, scatter forward and scatter backward light, resulting in attenuation of the light absorption and scattering phenomena. To wit:

$$t(x) = e^{-\beta d(x)} \tag{2}$$

In this model, $d(x)$ denotes the scene depth and β denotes the attenuation coefficient. The transmittance decays exponentially with depth. Adrian Galdran modified Koschmieder's attenuation model by calculating the red channel independently to make it more consistent with the imaging characteristics of underwater environments. The RDCP theory [17] is:

$$1 - I^R = t\left(1 - J^R\right) + \left(1 - t\right)\left(1 - A^R\right) \tag{3}$$

$$J^{RED}(x) := \min \left\{ \begin{array}{l} \min\limits_{y \in \Omega(x)} \left(1 - J^R(y)\right) \\ \min\limits_{y \in \Omega(x)} \left(J^G(y)\right) \\ \min\limits_{y \in \Omega(x)} \left(J^B(y)\right) \end{array} \right\} \approx 0 \tag{4}$$

where I^R denotes the red channel value of the original underwater image, J^R denotes the red channel value of the restored image, A^R represents the atmospheric light intensity in the red channel, J^{RED} denotes the red dark channel image, and J^G is the green channel value of the restored image, and J^B is the blue channel value of the restored image. Assuming that the blurring of the underwater image is distance-dependent, the estimated value of the background light naturally corresponds to the maximum value of the red channel of the original image.

Furthermore, interference from artificial light sources is a common challenge when dealing with underwater images, especially in calculations where transmittance is considered. Artificial light sources usually cause color distortion, leading to degradation of image quality. To effectively deal with this problem, the effect of artificial light sources first needs to be properly understood and quantified. Therefore, saturation is defined as the purity of pixel chromaticity, which serves as an important metric to distinguish between artificial illumination and natural light. In a natural lighting environment without artificial illumination, a higher saturation of colors means that the colors are close to the pure spectrum. On the contrary, the presence of artificial lighting often leads to a decrease in the saturation of pixels. Therefore, the degree of lack of saturation can distinguish between artificial and natural lighting. Transmittance can be defined as:

$$Sat(I) = \frac{\max\left(I^R, I^G, I^B\right) - \min\left(I^R, I^G, I^B\right)}{\max\left(I^R, I^G, I^B\right)} \tag{5}$$

$$t(x) = 1 - \min\left\{ \begin{array}{l} \dfrac{\min\limits_{y\in\Omega(x)} (1 - I^R(y))}{1 - A^R}, \dfrac{\min\limits_{y\in\Omega(x)} I^G(y)}{A^G} \\ \dfrac{\min\limits_{y\in\Omega(x)} I^B(y)}{A^B}, \lambda \min\limits_{y\in\Omega(x)} Sat(y) \end{array} \right\} \tag{6}$$

where Sat represents the saturation of the pixel. The adjustment formula for the transmittance $t(x)$ utilizes the saturation Sat metric, a method that allows the calculation of transmittance to depend not only on the intensity of a single pixel, but to more fully consider the lighting environment of the entire image. The coefficient λ takes the value of $[0,1]$ and is used to adjust the proportion of artificial lighting in the image. Typically, it is set to the average of $1 - Sat$ to fit the artificial lighting under consideration. The A^G and A^B denote the intensity of illumination for the green and blue channels, respectively, which reflects the different sensitivities of the different color channels to the artificial light source, thus allowing for a more accurate color recovery.

II. B. Theories related to image processing algorithms

II. B. 1) Retinex theory

In Retinex theory [18], [19], the color of an object is not determined by the absolute value of the intensity of the reflected light, but by the object's ability to reflect red, green, and blue light, and thus the color of the object is not affected by the non-uniformity of the illumination. The composition of an image in Retinex theory is shown in Figure 1. That is, the image signal S of an object viewed by an observer is determined by the incident illumination L_{ret} and the reflected light R_{ret} of the object itself, which carries the detailed information of the image.

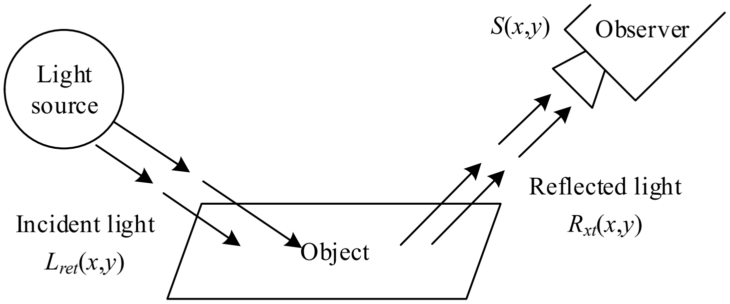

Figure 1: The composition of the image of the retinex theory

Retinex theory assumes that the original image signal S is the product of the incident illumination L_{ret} and the reflected light R_{ret} from the object itself, i.e:

$$S = L_{ret} R_{ret} \tag{7}$$

When utilizing Retinex theory, the image is usually transferred to the logarithmic domain such that the product relation is converted to a sum relation, i.e:

$$\log_2 S = \log_2 \left(L_{ret} R_{ret}\right) = \log_2 L_{ret} + \log_2 R_{ret} \tag{8}$$

In the underwater image brightness enhancement process, the incident light illuminance L_{ret} can be estimated from the original image S, and the L_{ret} component can be further removed to obtain the original reflected light component R_{ret}, so as to eliminate the effect of brightness unevenness, and to realize the brightness enhancement of the underwater image. The overall effect of underwater image is improved.

II. B. 2) Gamma Correction

The gamma correction, also known as the power-law transformation, is defined by the power-exponential function:

$$V_{out} = V_{in}^{\gamma} \tag{9}$$

where, V_{out} is the gray value of the output image; V_{in} is the gray value of the input image; and γ is the power index coefficient of the gamma function.

Since the sensitivity of the human eye to an external light source has a power-index relationship with the input light intensity, and the camera sensitivity has a linear relationship with the input light intensity, in order to facilitate the human eye to recognize the image and to preserve the image brightness information more effectively, the shape of the gamma power-index function is changed by adjusting the gamma-corrected variable parameter to change the contrast and brightness of the image. In addition, this feature can also be used for dynamic estimation of unknown variables.

II. C. Improvement of Retinex's underwater image enhancement technique

II. C. 1) Overall network structure

In this paper, a low illumination underwater image enhancement framework is proposed in conjunction with Retinex theory to address the complex degradation caused by the problems of low brightness, obscure regional features and blurred details in underwater images. The degradation restorer is used to solve the degradation problem in the brightening image, and its core component is the light-directed variable attention module (LDAT) to enhance the perception of dark light regions, and the spatial-frequency-domain feature fusion module (SDFF) and the medium transfer module (MTM) are designed to improve the recovery of the distortion of underwater images.

According to Retinex theory, the image $I \in \mathbb{R}^{H\times W\times 3}$ can be decomposed into a dot product of the reflection component $R \in \mathbb{R}^{H\times W\times 3}$ and the incident component $L \in \mathbb{R}^{H\times W\times 3}$, but it cannot take into account the complex degradation in underwater low-light scenes. Therefore, in this paper, a perturbation term is added to the reflective component R and the incident component L to simulate the underwater imaging scene with the following equations:

$$I = R \odot L = \left(R+\hat{R}\right) \odot \left(L+\hat{L}\right) = R \odot L + R \odot \hat{L} + \hat{R} \odot \left(L+\hat{L}\right) \tag{10}$$

where $\hat{R} \in \mathbb{R}^{H\times W\times 3}$ and $\hat{L} \in \mathbb{R}^{H\times W\times 3}$ denote the perturbation terms. To obtain a clear underwater image, multiply a luminance map $\bar{L} \in \mathbb{R}^{H\times W\times 3}$ by a simultaneous dot on both sides of the equation such that $\bar{L} \odot L = 1$, i.e.:

$$I_{lu} = I \odot \bar{L} = R + R \odot \left(\hat{L} \odot \bar{L}\right) + \left(\hat{R} \odot \left(L+\bar{L}\right)\right) \odot \bar{L} = R + C \tag{11}$$

where $I_{\mathrm{lu}} \in \mathbb{R}^{H\times W\times 3}$ denotes the brightened image, $R \odot \left(\hat{L} \odot \bar{L}\right)$ denotes the underexposure, overexposure, and color aberration caused by the brightening process, $\left(\hat{R} \odot \left(L+\bar{L}\right)\right) \odot \bar{L}$ denotes noise and artifacts hidden in underwater low-light environments, and $C \in \mathbb{R}^{H\times W\times 3}$ denotes overall degradation of low-light underwater images.

II. C. 2) Light-guided variable attention modules

LDAT consists of a light-directed multi-head attention mechanism (LD-MSA) [20] and a feed-forward network (FFN), with CB operations inserted at the end of the FFN to support the intensive interaction requirements of the visual Transformer and to enhance the generalization of the module.

LD-MSA mechanism: firstly, a uniform mesh is generated by downsampling according to the input feature map as a reference point, the query vector q is obtained by linear projection of the input feature x by the fully connected layer (fc), and multiple sets of offsets are learned by input into the offset network, so as to adjust the position of the sampling point to adapt to different brightness distributions, and the size of $\tilde{x}$ is obtained by using bilinear interpolation and x to obtain the size unification, and then the deformed key vector $\tilde{k}$ is obtained through linear projection and the value vector $\tilde{v}$, the process is:

$$\begin{aligned} &q = xW_q, \tilde{k} = \tilde{x}W_k, \tilde{v} = \tilde{x}W_v \\ &\Delta p = \theta_{offset}\left(q\right), \tilde{x} = \phi\left(x; p+\Delta p\right) \end{aligned} \tag{12}$$

where, W_q, W_k, W_v denote the projection matrix; θ_{offset} indicates the offset network; Δp represents the offset, which is the same size as the reference point; ϕ represents bilinear interpolation; p represents a uniform mesh $\left\{\left(p_x, p_y\right) | \left(0,0\right), \cdots, \left(W_{\mathrm{G}}-1, H_{\mathrm{G}}-1\right)\right\}$, and its position is based on size $H_G \times W_G$ to $[-1,+1]$, $[-1,-1]$ for the lower left corner, and $[+1,+1]$ for the upper right corner.

The luminance feature F_{lu} is input into each LD-MSA of the LDAT, and the LD-MSA treats a single channel of the feature map as a token, then calculates the similarity between q and $\tilde{k}$, and weights the $\tilde{v}$ of the aggregate luminance feature l, and the self-attention of the m head is:

$$Z_m = \sigma\left(\frac{q_m \tilde{k}_m^T}{\alpha_m} + R\right)\left(\tilde{v}_m \square\ l_m\right) \tag{13}$$

where, α_m denotes a one-dimensional learnable parameter for adaptive control of the attention weights of each head; R denotes the relative position encoding, and to be consistent with the size of $\tilde{v}$, a convolution is used to match the spatial size. Finally, the self-attention of each head is spliced and projected through W_0 to obtain the final attention graph, i.e:

$$Attention = Concat\left(Z_1, \cdots, Z_m\right)W_0 \tag{14}$$

II. C. 3) Air-frequency domain feature fusion module

The SDFF module is divided into two parts: frequency domain processing and spatial domain processing. The frequency domain part utilizes the Fourier transform to convert to the frequency domain space, after a convolutional layer to determine the weight of each frequency component to improve the accuracy of capturing the lines and edges of the underwater image, and finally the Fourier inverse transform is performed to obtain the information. For a given input feature F :

$$F_f = f_{IFFT}\left(\sigma\left(f_1\left(f_{FFT}\left(\mathrm{F}\right)\right)\right)\right) \tag{15}$$

where, f_{FFT} denotes the Fast Fourier Transform, f_{IFFT} denotes the Fast Fourier Inverse Transform, f_1 denotes the convolution plus batch normalization operation, σ denotes the Relu function, and F_f is the output of the frequency domain part. Namely:

$$F_s = f_4\left(f_2\left(\mathrm{F}\right)\square\ \sigma\left(\mathrm{F} + Up\left(f_3\left(AvgPool\left(\mathrm{F}\right)\right)\right)\right)\right) \tag{16}$$

where, $AvgPool$ denotes average pooling, f_2, f_3, f_4 denote convolution plus batch normalization operations, Up denotes bilinear interpolation, σ denotes the Sigmoid function, and F_s is the spatial domain output. Finally, the feature maps in the frequency and spatial domains are spliced in the channel dimension, and the output is obtained by feature fusion through point-by-point convolution, i.e:

$$Output = f_{pw}\left(F_f + F_s\right) \tag{17}$$

II. C. 4) Media transfer module

In this paper, we propose a media transport module based on the underwater dark channel prior, which is embedded in the jump junctions of the codec structure and weights the features extracted at each layer of the encoder by the media transport map as a way of boosting the response in regions of higher quality degradation, viz:

$$Output = \mathrm{F} \oplus \mathrm{F}\ \square\ \sigma\left(f(T)\right) \tag{18}$$

where, T denotes the medium transport map, F denotes the input features, f denotes the convolution operation, and σ denotes the Sigmoid function. The complexity of the underwater environment and the uncertainty of underwater noise lead to an initial error in the medium transport map estimated by the network. Therefore, a priori based algorithm is used to obtain the medium transport map, which can be derived as follows based on the underwater imaging model:

$$T(x) = 1 - \min_{y \in \Omega(x)}\left(\min_{c} \frac{I_c(y)}{A_c}\right) \tag{19}$$

where, $I_c(y)$ denotes any color channel of the underwater image; $\Omega(x)$ denotes a window centered at pixel point x; and A_c denotes the global background light, which is estimated using the dark channel map. Inspired by the robust underwater dark channel prior, this paper considers only the green and blue channels of the image, and this prior knowledge can be defined as:

$$UDCP(x) = \min_{y \in \Omega(x)}\left(\min_{c \in \{g,b\}}\left(I_c(y)\right)\right) \tag{20}$$

The minimum value of each pixel on both channels is then smoothed using a minima filter to obtain an underwater dark channel image corresponding to the original underwater image.

III. Analysis of the results based on the image outgrowth of the reed root system at different water levels

III. A. Experiments and analysis of results

In order to better confirm the effectiveness of the algorithm in this paper, three typical underwater images of reed roots in a sea ranch were selected for processing and compared and analyzed with the dark channel algorithm and MSR algorithm. Experimental environment: In August 2024, in the artificial reef area of M province, the temperature is about 22.5 ℃ . Equipment conditions:The operating system Windows, the software platform is MATLAB.Experimental data:The camera GoPro was used to take pictures of the sea ranch, and the data size was 1,955×1,150, and the Ado-be Premiere software was used to intercept each frame in the video, and then the image size was transformed to the appropriate size of 355×345.Experimental parameters:Segmented linear stretching of the The slope is determined by the selected interval, and different images correspond to different intervals. When the slope is larger, the image is whitish and the contrast is reduced; when the slope is smaller, the image is darker and the contrast is reduced, so it is important to choose the appropriate stretching interval according to the image characteristics. According to the size of the image to select the number of chunks that can be divided, ClipLimit default value of 0.05, the larger the value of the greater contrast, when the value is too large, there will be a checkerboard effect.

Tests are done on the above algorithms separately, and the results of information entropy and standard deviation comparison are shown in Table 1. The results show that, evaluated from subjective vision, after the comparison of three algorithms, the algorithm of this paper retains the real color of the image on the basis of removing the color difference, increases the contrast of the image, effectively removes the backward scattering phenomenon existing in the underwater image, and makes up for the defects of the lack of underwater light. In addition, the information entropy and standard deviation of the original image are relatively low, and their values are greatly improved after processing by the algorithm in this paper. The standard deviation of all three images after processing by the dark channel a priori algorithm is smaller than that of the MSR method, but their information entropy is larger than that of the MSR method. After processing by this paper's method, the information entropy of image 3 rises from 6.762 to 7.827 and the standard deviation rises from 18.978 to 58.973. Throughout the whole, except for the information entropy value of image 1 after processing by this paper's algorithm which is slightly smaller than that of the dark-channel a priori algorithm, this paper's algorithm is the best in terms of information entropy and standard deviation. Considering subjective vision and objective data comprehensively, this paper's algorithm has better applicability.

Table 1: Information entropy and standard deviation

Algorithm	Standard deviation			Information entropy		
	Figure 1	Figure 2	Figure 3	Figure 1	Figure 2	Figure 3
Original drawing	27.218	30.301	18.978	7.175	7.243	6.762
Dark channel priori	31.979	40.976	26.993	7.305	7.446	7.275
MSR	30.989	39.007	42.011	7.226	7.333	7.201
This method	40.042	52.981	58.973	7.331	7.507	7.827

In order to further illustrate the superiority of this paper's algorithm, the grayscale histograms of the images processed by the three algorithms are compared and analyzed, respectively.The comparative results of the grayscale histograms under the three methods are shown in Fig. 2, in which (a)~(d) represent the original image, the dark-channel a priori algorithm, the MSR and this paper's method, respectively.

If the uniformity of the histogram distribution of an image is better, the image quality is better. It can be seen that due to the low contrast of the original image, the overall brightness is on the dark side, thus resulting in a very uneven distribution of the gray level histogram of the original image. After processing by several algorithms, the grayscale histogram distribution is improved, and the original more concentrated grayscale interval becomes uniform. After comparison, it is found that the grayscale histogram of the image processed by the algorithm in this paper has the best distribution uniformity, and the image is the clearest and has the highest contrast.

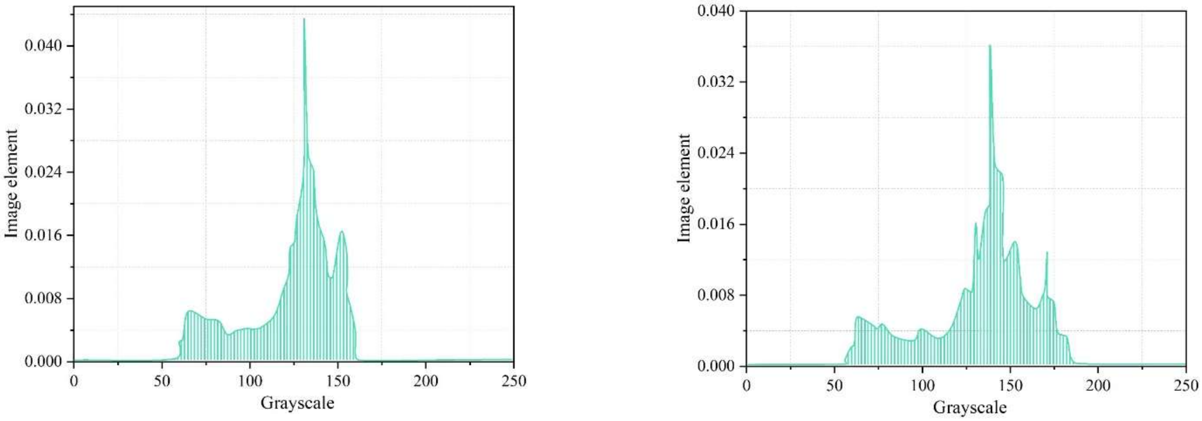

(a)Original drawing (b)Dark channel transcendental algorithm

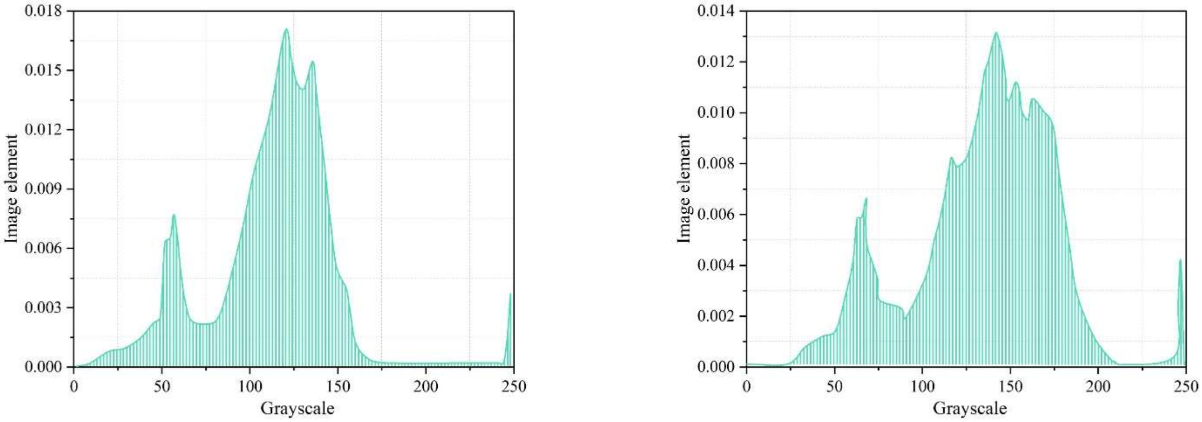

(c)MSR (d)This method

Figure 2: The comparison results of the grey histogram under three methods

III. B. Image Quality Analysis

Evaluation using quality assessment metrics of images is more convincing than subjective evaluation by human eyes. The results of the algorithm processing are evaluated using 3 quality metrics: underwater image quality metric (UIQM), information entropy, and point sharpness (EAV). Three images were evaluated using the three image quality metrics and the results of underwater image quality evaluation are shown in Table 2. The dark channel a priori algorithm does not improve the UIQM, information entropy and EAV indexes of the image much, even slightly lower than the original image, and the contrast and sharpness of the image are reduced.The MSR algorithm improves the image quality more obviously, and the information entropy of the image in the processed portion of the MSR algorithm is slightly better than that of all algorithms of the experiments.The image enhanced by the MSR algorithm still has a large chromatic aberration, which has an effect on the UIQM indexes.

The UIQM, information entropy and EAV indexes of this paper's algorithm are basically better than those of the two comparative algorithms, and the clarity index EAV is much higher than that of all the experimental algorithms, and the UIQM indexes are higher than that of all the algorithms, which effectively corrects the color deviation of the image, and enhances the clarity and contrast of the image.

Table 2: Underwater image quality evaluation results

Method	Experimental method	Figure 1	Figure 2	Figure 3
Dark channel priori	UIQM	1.911	4.323	3.875
	Information entropy	4.342	4.384	4.61
	EAV	3.958	6.435	10.352
MSR	UIQM	1.347	4.383	3.984
	Information entropy	4.647	4.864	4.997
	EAV	8.783	14.333	21.117
This method	UIQM	2.076	4.594	4.057
	Information entropy	4.189	4.416	4.349
	EAV	5.894	11.599	17.085

The average running time of different algorithms is shown in Table 3. Meanwhile, from the average running time of different algorithms, it can be seen that the running time of this paper's algorithm is shorter compared to the dark channel a priori algorithm and MSR algorithm, which shows that this paper's running method is better.

Table 3: Average running time of different algorithms

Running time	Algorithm		
	Dark channel priori	MSR	This method
Mean length(s)	71.49	19.074	6.696

III. C. Anatomy of reed root system under different water level conditions

In this paper, we take the reeds in the nature reserve as the research object, and use the method of the previous paper to obtain the changes of the anatomical structure of the reed root system under different water depths. In this way, the changes of reed root anatomy under different water depth gradients are investigated.

III. C. 1) Aeration organization of reed root cortex at different water depths

The correlation between the proportion of root aeration tissue and water depth of reed is shown in Figure 3. According to the results of linear fitting, it can be seen that the proportion of root cortical aerial tissue of reed and water depth were significantly and positively correlated at different points ($P < 0.05$, Sample point 1: $R^2 = 0.9013$; Sample point 2: $R^2 = 0.9127$; Sample point 5: $R^2 = 0.9288$), and the proportion of root cortical aerial tissue of reed increased with water depth under the condition of water depth of 0cm-35cm. The proportion of aeration tissue in the root cortex of reed varies in different sample sites, even at the same water depth. The proportion of aerated tissue in the root cortex of deeply flooded reeds (water depth > 25 cm) was significantly greater than that of non-flooded reeds in all sample sites ($P < 0.05$).

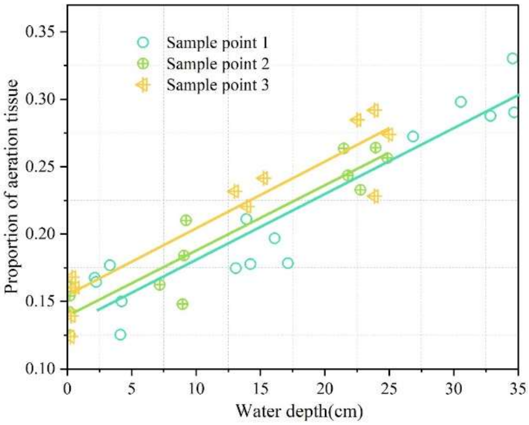

Figure 3: Correlation between root ventilation and depth

III. C. 2) Effect of different water depths on reed root diameter

The ratio of mid-column diameter to root diameter of reed roots at different points is shown in Fig. 4. It can be seen that the ratio of root mid-column diameter to root diameter of reed differed at different water depths ($P < 0.05$). At water depth of 0 cm, the ratio of root mid-column diameter to root diameter of reed was significantly greater than that at medium water level (water depth of 10 cm) ($P < 0.05$), which proved that water deficit would lead to an increase in the ratio of root mid-column diameter to root diameter of reed; meanwhile, at deep flooding (water depth of >25 cm) in both Sample Points 1 and 2, the ratio of root mid-column diameter to root diameter of reed was significantly greater than that at medium water depth (water depth of >25 cm). Meanwhile, in deep flooding (water depth > 25 cm), the ratio of root mid-column diameter to root diameter was significantly greater than the ratio of root mid-column diameter to root diameter in mid-water reed in Sample Site 1 and Sample Site 2 ($P < 0.05$), while in Sample Site 3, there was no significant difference in the ratios of root mid-column diameter to root diameter between the deeply flooded and mid-watered reed in Sample Site 3 ($P > 0.05$).

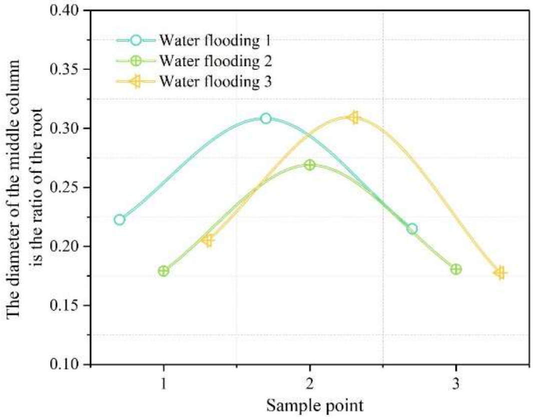

Figure 4: The diameter of the middle column is compared to the diameter of the root

IV. Conclusion

The image processing algorithm of underwater reed root system based on the improved Retinex theory performs well in several performance indexes. The images processed by the algorithm far exceeded the comparison method in terms of the clarity index EAV, in which the EAV values of Image 1, Image 2 and Image 3 reached 5.894, 11.599 and 17.085, respectively, which were significantly better than those of the traditional algorithm. The UIQM index of underwater image quality metric is also excellent, with the UIQM values of 2.076, 4.594 and 4.057 for the three test images, which effectively corrects the problem of image color deviation. In terms of algorithm operation efficiency, the average processing time is only 6.696 seconds, compared with 71.49 seconds for the dark-channel a priori algorithm and 19.074 seconds for the MSR algorithm, which is a significant improvement in processing speed. Through in-depth analysis of the anatomical structure of the reed root system, it was found that there was a significant positive correlation between the proportion of root cortex aerated tissues and the water depth, and the correlation coefficient R^2 values exceeded 0.90 at different points, indicating that the change of water depth has an important effect on the root system structure. The algorithm not only solves the technical problem of poor quality of underwater images, but also provides a reliable tool for quantitative analysis of plant root structure, which is of great value to promote the study of wetland ecology and the exploration of the adaptive mechanism of aquatic plants.

References

[1] Mao, D., Wang, Z., Wu, J., Wu, B., Zeng, Y., Song, K., ... & Luo, L. (2018). China's wetlands loss to urban expansion. Land degradation & development, 29(8), 2644-2657.

[2] Zou, Y., Wang, L., Xue, Z., E, M., Jiang, M., Lu, X., ... & Yu, X. (2018). Impacts of agricultural and reclamation practices on wetlands in the Amur River Basin, Northeastern China. Wetlands, 38, 383-389.

[3] Zhao, X., Zhang, Q., He, G., Zhang, L., & Lu, Y. (2021). Delineating pollution threat intensity from onshore industries to coastal wetlands in the Bohai Rim, the Yangtze River Delta, and the Pearl River Delta, China. Journal of Cleaner Production, 320, 128880.

[4] Asaad, A. A., El-Hawary, A. M., Abbas, M. H., Mohamed, I., Abdelhafez, A. A., & Bassouny, M. A. (2022). Reclamation of wastewater in wetlands using reed plants and biochar. Scientific Reports, 12(1), 19516.

[5] Čížková, H., Kučera, T., Poulin, B., & Květ, J. (2023). Ecological basis of ecosystem services and management of wetlands dominated by common reed (Phragmites australis): European perspective. Diversity, 15(5), 629.

[6] Balwan, W. K., & Kour, S. (2021). Wetland-an ecological boon for the environment. East African Scholars Journal of Agriculture and Life Sciences, 4(3), 38-48.

[7] Tupach, S. O., Kandeel, S. E., Kherallah, I. A., El-Saied, H., & Nasser, R. A. S. (2022). Potential of using two types of reed for pulp and paper industry. Alexandria Science Exchange Journal, 43(2), 373-384.

[8] Caponetto, R., Cuomo, M., Detommaso, M., Giuffrida, G., Presti, A. L., & Nocera, F. (2023). Performance assessment of Giant Reed-based building components. Sustainability, 15(3), 2114.

[9] Amri, A. E., Bensalah, J., Essaadaoui, Y., Lebkiri, I., Abbou, B., Zarrouk, A., ... & Lebkiri, A. (2022). Elaboration, characterization and performance evaluation of a new environmentally friendly adsorbent material based on the reed filter (Typha Latifolia): Kinetic and thermodynamic studies and application in the adsorption of Cd (II) ion. Chemical Data Collections, 39, 100849.

[10] Zhang, D., Jiang, Q., Liang, D., Huang, S., & Liao, J. (2021). The potential application of giant reed (Arundo donax) in ecological remediation. Frontiers in Environmental Science, 9, 652367.

[11] Heneberg, P., Bogusch, P., Tauchmanová, P., Řezáč, M., & Astapenková, A. (2017). Common reed (Phragmites australis) gall as the limiting nesting resource of rare wetland bees and wasps (Hymenoptera: Aculeata & Evanioidea) in Central Europe. Ecological Engineering, 108, 100-113.

[12] Tao, J., Zhang, Y., Zhang, T., You, Z., Shah, K. J., & Kim, H. (2022). Application of reeds as carbon source for enhancing denitrification of low C/N micro-polluted water in vertical-flow constructed wetland. Applied Sciences, 12(13), 6756.

[13] Doležal, J., Kučerová, A., Jandová, V., Klimeš, A., Říha, P., Adamec, L., & Schweingruber, F. H. (2021). Anatomical adaptations in aquatic and wetland dicot plants: Disentangling the environmental, morphological and evolutionary signals. Environmental and Experimental Botany, 187, 104495.

[14] Li, S., Lu, S., Wang, J., Chen, Z., Zhang, Y., Duan, J., ... & Guo, J. (2023). Responses of physiological, morphological and anatomical traits to abiotic stress in woody plants. Forests, 14(9), 1784.

[15] Ngernsaengsaruay, C., Puangsin, B., Leksungnoen, N., Khantayanuwong, S., Chanton, P., Thaepthup, T., ... & Banjatammanon, N. (2023). Morphology, Taxonomy, Culm Internode and Leaf Anatomy, and Palynology of the Giant Reed (Arundo donax L.), Poaceae, Growing in Thailand. Plants, 12(9), 1850.

[16] Lázaro, W. L., Oliveira-Júnior, E. S., Silva, C. J. D., Castrillon, S. K. I., & Muniz, C. C. (2020). Climate change reflected in one of the largest wetlands in the world: an overview of the Northern Pantanal water regime. Acta Limnologica Brasiliensia, 32, e104.

[17] Shin Hyuk Hwang,Se Kil Park,Sung Hyun Park,Ki Won Kwon & Tae Ho Im. (2023). RDCP: A Real Time Sea Fog Intensity and Visibility Estimation Algorithm. Journal of Marine Science and Engineering,12(1),

[18] Yue Sun,Yutao Jin,Xiaoyan Chen,Yanbin Xu,Xiaoning Yan & Zefu Liu. (2025). Unsupervised detail and color restorer for Retinex-based low-light image enhancement. Engineering Applications of Artificial Intelligence,153,110867-110867.

[19] Rongtai Cai & Helin Que. (2025). Brain-like contour detector following Retinex theory and Gestalt perception grouping principles. Neurocomputing,633,129765-129765.

[20] Li Li,Huanyu Li & Peng Ren. (2025). Underwater image captioning via attention mechanism based fusion of visual and textual information. Information Fusion,123,103269-103269.